Theor Chem Acc (2012) 131:1214
DOI 10.1007/s00214-012-1214-y

REGULAR ARTICLE

# Structure and electronic properties of hydrated mesityl oxide: a sequential quantum mechanics/molecular mechanics approach

**Marcus V. A. Damasceno · Benedito J. Costa Cabral · Kaline Coutinho**

Received: 14 February 2012 / Accepted: 24 March 2012 / Published online: 22 April 2012


**Abstract** The hydration of mesityl oxide (MOx) was investigated through a sequential quantum mechanics/molecular mechanics approach. Emphasis was placed on the analysis of the role played by water in the MOx *syn*–*anti* equilibrium and the electronic absorption spectrum. Results for the structure of the MOx–water solution, free energy of solvation and polarization effects are also reported. Our main conclusion was that in gas-phase and in low-polarity solvents, the MOx exists dominantly in *syn*-form and in aqueous solution in *anti*-form. This conclusion was supported by Gibbs free energy calculations in gas phase and in-water by quantum mechanical calculations with polarizable continuum model and thermodynamic perturbation theory in Monte Carlo simulations using a polarized MOx model. The consideration of the in-water polarization of the MOx is very important to correctly describe the solute–solvent electrostatic interaction. Our best estimate for the shift of the $\pi$–$\pi^*$ transition energy of MOx, when it changes from gas-phase to water solvent, shows a red-shift of $-2{,}520 \pm 90$ cm$^{-1}$, which is only 110 cm$^{-1}$ (0.014 eV) below the experimental extrapolation of $-2{,}410 \pm 90$ cm$^{-1}$. This red-shift of around $-2{,}500$ cm$^{-1}$ can be divided in two distinct and opposite contributions. One contribution is related to the *syn* → *anti* conformational change leading to a blue-shift of $\sim 1{,}700$ cm$^{-1}$. Other contribution is the solvent effect on the electronic structure of the MOx leading to a red-shift of around $-4{,}200$ cm$^{-1}$. Additionally, this red-shift caused by the solvent effect on the electronic structure can by composed by approximately 60 % due to the electrostatic bulk effect, 10 % due to the explicit inclusion of the hydrogen-bonded water molecules and 30 % due to the explicit inclusion of the nearest water molecules.

**Keywords** Solvent effect 1 · Theoretical calculations 2 · Absorption electronic spectrum 3

## 1 Introduction

A better understanding of solvent effects on molecular properties is of fundamental interest for explaining the mechanisms and dynamics of chemical and biochemical processes in solution [1, 2]. The knowledge of these mechanisms at the molecular level may have a strong impact on the design of biochemical and technological applications. Solvent effects may influence the properties of a solvated species in many different ways. They may affect, in particular, the conformational equilibrium relative to the gas-phase or low-polarity solvent [3, 4]. This effect can be explained, in general, by the free energy difference between conformations in solution, mainly in polar solvents, where it is expected that structures with a larger dipole moment are favored [5]. Solvents effects are also very important for understanding the vibrational and

Dedicated to Professor Marco Antonio Chaer Nascimento and published as part of the special collection of articles celebrating his 65th birthday.

**Electronic supplementary material** The online version of this article (doi:10.1007/s00214-012-1214-y) contains supplementary material, which is available to authorized users.

M. V. A. Damasceno · K. Coutinho (✉)
Instituto de Física, Universidade de São Paulo, CP 66318, São Paulo, SP 05314-970, Brazil
e-mail: kaline@if.usp.br

B. J. Costa Cabral
Grupo de Física Matemática da Universidade de Lisboa, Av. Professor Gama Pinto 2, 1649-003 Lisbon, Portugal

electronic spectra in solution [6]. It is well-known that the electronic absorption spectra in solution may, in comparison with gas-phase data, exhibit significant changes in the position, intensity and shape of the absorption bands [1, 6–8]. These changes are related, in general, to the solvent polarity although some specific local interactions (e.g. hydrogen bonding) are also important. The concept of solvatochromism was adopted for describing the change relative to gas phase in the position of the maximum absorption wavelength, $\lambda_{max}$, that can be related, in many cases, to the polarity of a particular solvent. In this context, hypsochromic [bathochromic] shifts are associated with a blue [red]-shift of $\lambda_{max}$. Solvatochromic effects are driven by solute–solvent interactions. Therefore, the understanding of these effects depends on the analysis of different contributions to the solvent–solute interactions, including specific intermolecular contributions [9]. The solvent polarity has been studied through the transition energy of solvatochromic dyes, which exhibit absorption bands in the visible that are shifted with respect to the solvent [10]. Therefore, in this way, it was possible to define empirical parameters for the solvent polarity through UV–vis measurements for a large number of solvatochromic species with the purpose of establishing an empirical scale of solvent polarities. This procedure, actually, led to the definition of different polarity scales [1, 11–13].

The main purpose of the present work is to investigate the role played by solvent effects on the conformational stability and electronic spectrum of the mesityl oxide (MOx) molecule [$(CH_3)_2C{=}CHCOCH_3$, 4-methyl-3-penten-2-one] through theoretical calculations. The MOx can be considered as a model for larger species of ketones characterized by the presence of a carbonyl (–C=O) group linked to other two organic groups with a general formula RC–C(=O)–CR′. It should be observed that the presence of low-wavelength (high-energy) electronic transitions sensitive to the solvent polarity in non-saturated α,β-ketones makes these systems very important for understanding solvatochromic effects. Five isomers of the MOx can exist. The conjugate acetonic form, characterized by the presence of the –C=O group in a conjugate C–C=C- array, with two isomers (*syn* and *anti* or *cis* and *trans*) is illustrated in Fig. 1 (top). These two isomers differ by the relative orientation (torsional angle) of the C=C–C=O atoms. This torsional angle is 0° for the *syn*-isomer (*cis*) and 180° for the *anti*-isomers (*trans*). In the non-conjugate acetonic form, the isomer of oxide mesityl [4-methyl-4-penten-2-one] is named *iso*-mesityl oxide (IMOx) that can be also found in the *syn*- and *anti*-isomers, as illustrated in Fig. 1 (bottom). An enolic form for species with at least a α-hydrogen atom can be also identified. However, it was experimentally verified through the analysis of the vibrational spectrum that this enolic form is not present in

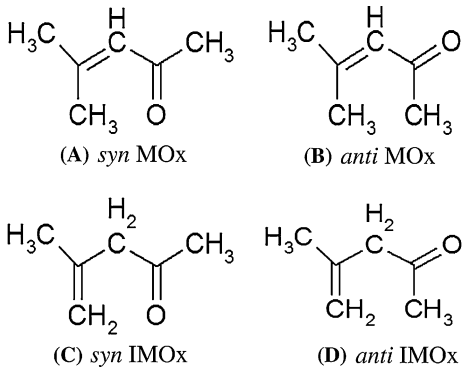


**Fig. 1** Chemical structure of *syn*- and *anti*-isomers of mesityl oxide (MOx) and of iso-mesityl oxide (IMOx)

equilibrium at normal conditions, but it was found a composition of 91 % of conjugated isomer (MOx) and 9 % of unconjugated isomer (IMOx) [14]. Experimental results for the vibrational (IR) and electronic absorption (UV–vis) spectra, as well as their dependence on thermodynamic properties (boiling points) of MOx and IMOx, have been reported [14, 15]. In the non-polar solvent iso-octane, MOx (b.p. = 130 °C) exhibits an intense IR absorption band associated with the C=O double bond in a conjugate position [14] and two UV–vis absorption bands at 231 nm (strong, $\pi$–$\pi^*$) and 329 nm (weak, $n$–$\pi^*$) [15, 16]. In the same solvent, the IMOx molecule (b.p. = 121.5 °C) shows an IR absorption band typical of a C=O bond in a non-conjugate position [14] and only one UV–vis absorption band at 290 nm (weak, $n$–$\pi^*$) [15]. Therefore, the low-lying $n$–$\pi^*$ absorption band in the region of 290–330 nm cannot be attributed to a specific isomer due to the presence of MOx and IMOx isomers in the experimental system. Additionally, for some solvents, like water and tetrafluoropropanol, the $n$–$\pi^*$ band is submerged in the $\pi$–$\pi^*$ band and its $\lambda_{max}$ cannot be measured [16]. Then, the $\pi$–$\pi^*$ absorption band in the region of 200–250 nm is used to characterize the MOx isomer [14, 15], like other molecules of the family of non-saturated α,β-ketones [17, 18] and α,β-aldehydes [19]. Kosower [16] reported the $\lambda_{max}$ for the $\pi$–$\pi^*$ band of the MOx in several solvents including iso-octane, $\lambda_{max} = 230.6 \pm 0.5$ nm $(43{,}365 \pm 90\ cm^{-1})$, and water, $\lambda_{max} = 242.6 \pm 0.5$ nm $(41{,}220 \pm 90\ cm^{-1})$. Therefore, the solvatochromic or bathochromic shift of the $\pi$–$\pi^*$ band of MOx is well-known when the solvent changes from iso-octane to water, that is $-2{,}145 \pm 90\ cm^{-1}$ $(-0.266 \pm 0.011$ eV). An interesting aspect cited by Kosower [16], as a private communication from Dr. M. C. Whiting from Oxford University, is that the equilibrium between *syn*- and *anti*-forms of the MOx is solvent dependent. In spite of this, no further investigation was conducted to confirm this aspect. As far as we know, there are no theoretical studies on this system which is a simple model for the large family of the conjugate ketones.

The present work is focused on the changes of the electronic properties of mesityl oxide (MOx) upon hydration using quantum mechanics (QM) and molecular mechanics (MM) in a sequential procedure [20, 21]. It is organized as follows. First, we present the theoretical approach and computational details. Gas-phase results for MOx are then reported. This is followed by the analysis of different properties of MOx in water including the structure of the solution (solvation shells), hydrogen bonding, polarization effects, dipole moments, Gibbs free energy difference between *syn–anti* MOx isomers, and electronic absorption of MOx. We conclude by stressing the importance of adopting quantum mechanics and molecular mechanics methods (QM/MM) to investigate the electronic properties of solvatochromic species in solution and also the different contributions of the solute–solvent interactions to the solvatochromic shift.

## 2 Computational methods and details

The gas-phase structure (see Fig. 1 top) and electronic properties of MOx were determined by carrying out calculations with different theoretical methods and basis-sets. Density functional theory (DFT) [22] with the B3LYP [23, 24] exchange–correlation functional, and Møller-Plesset second-order perturbation theory (MP2) [25, 26] were applied to investigate the gas-phase properties of MOx. These methods were used combined with the family of Pople basis-set, 6–31+G(d), 6–311+G(d,p) and 6-311++G(d,p) [27], and the family of Dunning correlated with consistent hierarchical basis-set, cc-pVDZ and aug-cc-pVxZ (x = D, T) [28]. The electronic excitation energies were determined through the application of time-dependent density functional theory (TDDFT) [29] with several approximations for the exchange–correlation functional including B3LYP and BHandHLYP as implemented in Gaussian program [30]. Some reference calculations for gas-phase excitation energies were carried out by using equation-of-motion-coupled cluster with single and doubles excitations (EOM-CCSD) [31].

The analysis of the properties of mesityl oxide in aqueous solution was based on the continuous and discrete models of the solvent. Here, we used the polarizable continuum model (PCM) [32, 33], and for the discrete model of the solvent, we performed the sequential use of quantum mechanics and molecular mechanics methods, S-QM/MM [20, 21]. In the S-QM/MM procedure, initially the liquid-phase configurations are sampled from molecular simulations, and after statistical analysis, only configurations with less than 10 % of statistical correlation are selected and submitted to quantum mechanical calculations. In our study, we used the Monte Carlo method (MC) with Metropolis sampling technique [34] to perform the liquid simulation. This sampling was carried out separately for the *syn*, *anti* and transition state (TS) structures of MOx in water. By adopting this approach, fully relaxed water structures around each different isomer and TS are generated for the statistical analysis. We assumed that the MOx structures in water are not significantly modified relative to the gas-phase ones (see discussion on gas-phase properties of MOx below). These structures (optimized at the B3LYP/6-31+G(d) level) were kept rigid during the MC sampling that was generated by the DICE program [35]. The MC sampling was carried out at normal conditions ($p = 1$ atm; $T = 298$ K) in the *NpT* ensemble for a system with one MOx molecule and $N = 500$ water molecules in a cubic box of $L \approx 24.9$ Å length and by applying periodic boundary conditions and image method. In the calculation of the pair-wise energy, the MOx interacts with all water molecules within a center-of-mass separation that is smaller than the cutoff radius $r_c = L/2$ (that is approximately 12.45 Å in this case). For separations larger than $r_c$, the long-range correction of the potential energy was calculated [36]. In each simulation, $15 \times 10^6$ MC steps were performed in the thermalization stage and $37.5 \times 10^6$ MC steps in the production stage.

Solute–water and water–water interactions were described by a Lennard-Jones intermolecular potential plus a Coulombic term described by the interactions between atomic point charges. Water was represented by the SPC model [37]. The choice of the Lennard-Jones parameters for the MOx was driven by the OPLS force field [38] (see Table 1). Although charges from the OPLS force field can also be used to describe the Coulombic contribution, different works pointed out the importance of taking into account the solute polarization by the solvent charges [39]. The Coulombic contribution was reparametrized by a polarization procedure taking into consideration the (SPC) charge background of the water molecules. However, to assess the importance of these effects in the specific case of MOx, three different charge distributions for the solute were considered: charges from the OPLS force field [38]; two other charges obtained from QM calculations with MP2/aug-cc-pVDZ level and using the fitting of the electrostatic potential with CHELPG procedure [40] for the isolated solute (gas-phase) and embedded in the electrostatic potential of the water background (polarized) using an iterative procedure in the sequential QM/MM scheme [39].

The Gibbs free energy of hydration, $\Delta G_x(aq)$, was calculated using the MC simulation coupled to the thermodynamic perturbation theory (TPT) [41–43], in which a series of MC runs is carried out. A system with one solute molecule and 1000 water molecules at normal conditions in the *NpT* ensemble was used for the TPT calculations. The

**Table 1** Parameters of the Lennard-Jones intermolecular potential ($\varepsilon$ in kcal/mol and $\sigma$ in Å) and different sets of atomic charges (in $e$) and dipole moment ($\mu$ in D) for mesityl oxide at optimized geometry with B3LYP/6-31+G(d)

| | OPLS | | | Gas phase | | Polarized in water | |
|---|---|---|---|---|---|---|---|
| | $\varepsilon$ | $\sigma$ | $q$ | $q_{syn}$ | $q_{anti}$ | $q_{syn}$ | $q_{anti}$ |
| C1 | 0.066 | 3.50 | 0.000 | 0.393 | 0.255 | 0.456 | 0.302 |
| C2 | 0.066 | 3.50 | −0.115 | −0.585 | −0.508 | −0.634 | −0.549 |
| C3 | 0.066 | 3.50 | 0.500 | 0.746 | 0.716 | 0.868 | 0.837 |
| O4 | 0.210 | 2.96 | −0.500 | −0.538 | −0.532 | −0.753 | −0.769 |
| C5 | 0.066 | 3.50 | −0.180 | −0.341 | −0.299 | −0.377 | −0.311 |
| C6 | 0.066 | 3.50 | −0.180 | −0.309 | −0.185 | −0.344 | −0.168 |
| C7 | 0.066 | 3.50 | −0.180 | −0.326 | −0.238 | −0.342 | −0.319 |
| H8 | 0.030 | 2.50 | 0.115 | 0.156 | 0.164 | 0.182 | 0.173 |
| H9 | 0.030 | 2.50 | 0.060 | 0.085 | 0.076 | 0.116 | 0.102 |
| H10 | 0.030 | 2.50 | 0.060 | 0.085 | 0.076 | 0.116 | 0.102 |
| H11 | 0.030 | 2.50 | 0.060 | 0.084 | 0.079 | 0.088 | 0.086 |
| H12 | 0.030 | 2.50 | 0.060 | 0.083 | 0.060 | 0.105 | 0.050 |
| H13 | 0.030 | 2.50 | 0.060 | 0.087 | 0.059 | 0.099 | 0.073 |
| H14 | 0.030 | 2.50 | 0.060 | 0.087 | 0.059 | 0.108 | 0.072 |
| H15 | 0.030 | 2.50 | 0.060 | 0.080 | 0.074 | 0.095 | 0.110 |
| H16 | 0.030 | 2.50 | 0.060 | 0.133 | 0.070 | 0.124 | 0.099 |
| H17 | 0.030 | 2.50 | 0.060 | 0.080 | 0.074 | 0.093 | 0.110 |
| $\mu$ | | | 3.63/3.10 *syn/anti* | 2.77 | 3.90 | 4.97 (3.85) | 6.96 (5.25) |

All the QM calculations were performed with MP2/aug-cc-pVDZ. For comparison, in parentheses, it is also presented the value of the dipole moment polarized with the water environment described with continuum model PCM

MOx–water interactions were the same as described above. In this case, we adopted the polarized representation of the MOx charges that takes into account the charge relaxation of MOx upon hydration. For each species, the Gibbs free energy of hydration was calculated, as usual, through a hypothetical process where the solute–water interactions are switched-off in several simulations using the double-wide sampling [42]. Four simulations were used to annihilate the Coulomb potential and six simulations to annihilate the Lennard-Jones potential. Therefore, in the total, 10 simulations were performed to vanish completely the solute molecule from the aqueous solution. Each simulation had $90 \times 10^6$ MC steps in the thermalization stage and $450 \times 10^6$ steps in production stage. More details about this procedure can be found in refs. [43, 44].

## 3 Results

### 3.1 Gas-phase properties of mesityl oxide

Full geometry optimization and vibrational frequency calculations in the gas phase of the *syn*-, TS- and *anti*-forms of the OM were performed at the B3LYP and MP2 level of theory with 6–31+G(d) and aug-cc-pVDZ basis-set. A true minimum was verified for the *syn*- and *anti*-forms, and the transition state was also confirmed with only one imaginary frequency. Theoretical data for the gas-phase-optimized geometry of MOx are presented in Table 2 for the *syn*- and *anti*-isomers (see Fig. 2). We are not aware of experimental data for the structure of mesityl oxide. As illustrated in Table 2, the optimized structures of MOx are not very dependent on the adopted theoretical methods and basis-sets. In addition, small differences are observed when we compare data for the *syn*- and *anti*-isomers. For example, at the MP2/aug-cc-pVDZ level, the C=O distances are quite similar, 1.237 Å of the *syn*-isomer and 1.240 Å for the *anti*-isomers. The geometry of the MOx was also optimized in water using the PCM model and one explicit water molecule (see Table 2). The MOx structure still not very dependent on the solvent model, but comparing to gas phase, the C=O distance stretched approximately 0.01 Å in the presence of water, as expected [45].

Results for the gas-phase dipole moment of MOx are presented in Table 3, where they are compared with experimental information [1, 16, 46, 47]. For the *syn*-isomers, our MP2/aug-cc-pVDZ value (2.80 D) practically coincides with experiment values (2.80 D [16], 2.79 D in benzene [46], 2.83 D in dioxane [46] and 2.85 D in carbon tetrachloride [47]). For the *anti*-isomer, our MP2/aug-cc-pVDZ value (3.97 D) is also in good agreement with the experimental estimations ($\sim$3.7 D [16] and 3.88 D [47]).

**Table 2** Data for the optimized structures of the mesityl oxide in *syn*- and *anti*-isomers

| | B3LYP/6-31+G(d) | | B3LYP/aug-cc-pVDZ | | MP2/aug-cc-pVDZ | |
|---|---|---|---|---|---|---|
| | *Syn* | *Anti* | *Syn* | *Anti* | *Syn* | *Anti* |
| *Bond lengths* | | | | | | |
| C1=C2 | 1.354 (1.357) | 1.354 (1.357) | 1.355 | 1.354 | 1.364 | 1.364 |
| C1–C6 | 1.509 (1.507) | 1.512 (1.510) | 1.507 | 1.510 | 1.510 | 1.512 |
| C2–H8 | 1.090 (1.091) | 1.089 (1.089) | 1.093 | 1.093 | 1.097 | 1.097 |
| C3=O4 | 1.228 (1.236) 1.235[a] | 1.229 (1.240) 1.236[a] | 1.226 | 1.227 | 1.237 | 1.240 |
| H8…O4 | 3.307 (3.307) | 2.423 (2.435) | 3.311 | 2.427 | 3.332 | 2.452 |
| C2…O4 | 2.405 (2.408) | 2.324 (2.325) | 2.404 | 2.324 | 2.419 | 2.330 |
| *Valence angles* | | | | | | |
| C2, C1, C6 | 119.9 (119.7) | 118.9 (118.6) | 119.9 | 118.9 | 119.8 | 119.0 |
| C1, C2, C3 | 128.3 (128.7) | 133.1 (132.5) | 128.1 | 132.9 | 127.9 | 131.5 |
| C2, C3, O4 | 124.7 (124.9) | 117.5 (117.5) | 124.7 | 117.5 | 124.7 | 117.8 |
| C2, C3, C5 | 115.0 (114.9) | 123.6 (123.9) | 115.0 | 123.4 | 114.6 | 122.8 |
| O4, C3, C5 | 120.3 (120.2) | 119.0 (118.6) | 120.3 | 119.0 | 120.8 | 119.4 |
| *Dihedral angles* | | | | | | |
| C6, C1, C2, C3 | 180.0 (180.0) | 180.0 (180.0) | 180.0 | 180.0 | 180.0 | 178.6 |
| C6, C1, C2, H8 | 0.0 (0.0) | 0.0 (0.0) | 0.0 | 0.0 | 0.0 | −1.7 |
| C7, C1, C2, C3 | 0.0 (0.0) | 0.0 (0.0) | 0.0 | 0.0 | 0.0 | −1.0 |
| C1, C2, C3, O4 | 0.0 (0.0) | 180.0 (180.0) | 0.0 | 180.0 | 0.0 | 173.5 |
| C1, C2, C3, C5 | 180.0 (180.0) | 0.0 (0.0) | 180.0 | 0.0 | 180.0 | −7.8 |

Bond distances in Å, valence and dihedral angles in degrees. In parenthesis, it is shown the results for the MOx geometry optimized in water with polarizable continuum model, PCM

[a] Results using the MOx geometry optimized in a complex with one hydrogen-bonded water molecule

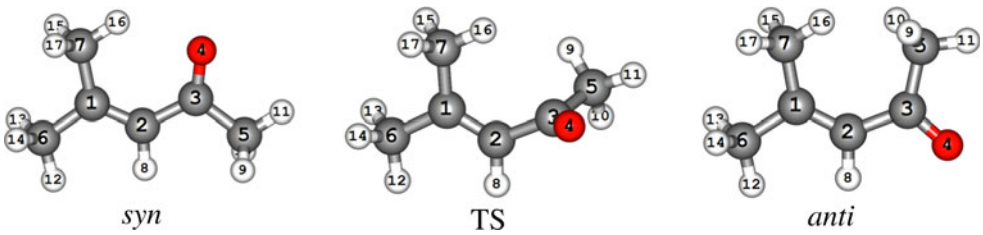


**Fig. 2** Illustration of the optimized geometry of *syn*- and *anti*-isomers, and the transition state (TS) of mesityl oxide. The atomic labels are shown

These results are consistent with other relevant information concerning on the gas-phase Gibbs free energy differences associated with the conformational change between the *syn*- and *anti*-isomers and the transition state (TS). These results are reported also in Table 3 and show that $\Delta G_{x\rightarrow y}(gas)$ is dependent on the theoretical method. Thus, MP2 free energy differences ($\Delta G_{syn\rightarrow anti}(gas) = 1.34$ kcal/mol and $\Delta G_{syn\rightarrow TS}(gas) = 3.57$ kcal/mol) are significantly lower than B3LYP predictions (2.20 and 5.93 kcal/mol, respectively). Based on the calculated values of $\Delta G_{syn\rightarrow anti}(gas)$ with different method, the population of the *anti*-isomer in gas phase was calculated and reported in the parenthesis. All used methods predict that the *syn*-isomer is more stable in the gas phase and the population of this particular isomer is large than 90 % in agreement with experimental findings [18, 19, 46–49].

Using the optimized geometry with B3LYP/6-31+G(d), the results for the dipole moment and relative free energy are close to those obtained with MP2/aug-cc-pVDZ. The calculated MOx dipole moment of the gas phase is 2.77 D for the *syn*-isomer and 3.90 D for the *anti*-isomers, and the relative free energy of the *anti*-isomer and of the transition state compared with the *syn*-isomer is 0.95 and 3.36 kcal/mol, respectively. Therefore, all further results reported in this work will be obtained using the geometry optimized with B3LYP/6-31+G(d) level.

The electronic absorption spectra of mesityl oxide in different solvents with different polarities ranging from

**Table 3** Gas-phase quantum mechanical dipole moments ($\mu$ in D) and Gibbs free energy changes ($\Delta G_{x\to y}$(gas) in kcal/mol) for the *syn*- and *anti*-isomers of mesityl oxide and for the transition state structure (TS)

| Dipole moment, $\mu$ | *Syn* | TS | *Anti* |
|---|---|---|---|
| B3LYP/6-31+G(d) | 3.14 | 3.30 | 4.38 |
| B3LYP/aug-cc-pVDZ | 3.00 | 3.22 | 4.29 |
| MP2/aug-cc-pVDZ | 2.80 | 3.00 | 3.97 |
| MP2/aug-cc-pVDZ[a] | 2.77 | 3.01 | 3.90 |
| Experimental | 2.80[b]; 2.79[c]; 2.83[d] | | ~3.7[b]; 3.88[d] |

| Relative free energy, $\Delta G_{x\to y}$(gas) | *Syn* → TS | *Syn* → *anti* |
|---|---|---|
| B3LYP/6-31+G(d) | 5.93 | 2.20 (2 %) |
| B3LYP/aug-cc-pVDZ | 6.80 | 2.00 (3 %) |
| MP2/aug-cc-pVDZ | 3.57 | 1.34 (9 %) |
| MP2/aug-cc-pVDZ[a] | 3.36 | 0.95 |

The experimental values for the dipole moment are also presented. The population of the *anti*-isomer in gas phase is reported in the parenthesis

[a] Geometry and thermal, enthalpy and entropic corrections at B3LYP/6-31+G(d) and electronic energy with MP2/aug-cc-pVDZ

[b] Ref. [16]

[c] In benzene [46]

[d] In carbon tetrachloride [47]

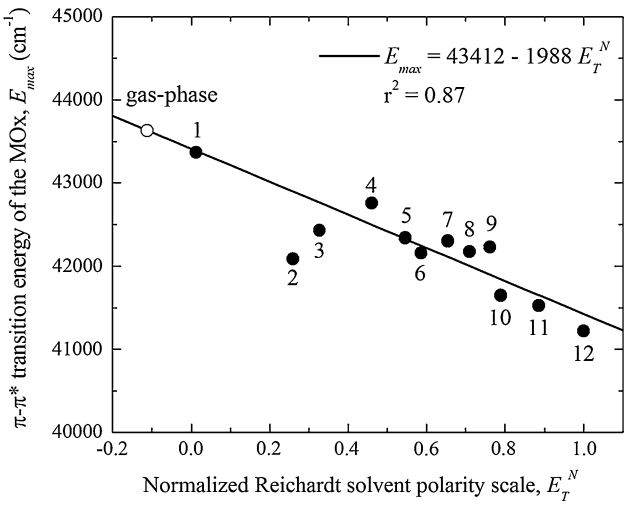


**Fig. 3** Extrapolation of the maximum absorption transition energy, $E_{max}$, of the mesityl oxide in gas phase, $E_T^N = -0.111$, as 43,630 cm$^{-1}$ (229.2 nm) using a linear regression in the plot of the experimental $E_{max}$ [16] versus the normalized Reichardt solvent polarity scale, $E_T^N$ [2]. The solvents and experimental values ($E_{max}$ and $E_T^N$) are (1) iso-octane (43,365 cm$^{-1}$ = 230.6 nm and 0.012), (2) chloroform (42,088 cm$^{-1}$ = 237.6 nm and 0.259), (3) ethylene dichloride (42,427 cm$^{-1}$ = 235.7 nm and 0.327), (4) acetonitrile (42,753 cm$^{-1}$ = 233.9 nm and 0.460), (5) isopropyl alcohol (42,337 cm$^{-1}$ = 236.2 nm and 0.546), (6) n-butyl alcohol (42,159 cm$^{-1}$ = 237.2 nm and 0.586), (7) ethanol (42,301 cm$^{-1}$ = 236.4 nm and 0.654), (8) 95 % ethanol (42,176 cm$^{-1}$ = 237.1 nm and 0.710), (9) methanol (42,230 cm$^{-1}$ = 236.8 nm and 0.762), (10) ethylene glycol (41,649 cm$^{-1}$ = 240.1 nm and 0.790), (11) tetrafluoropropanol (41,528 cm$^{-1}$ = 240.8 nm and 0.886) and (12) water (41,220 cm$^{-1}$ = 242.6 nm = and 1.000)

iso-octane (very low polarity, $E_T^N = 0.012$) to water (high polarity, $E_T^N = 1.000$) were determined by Kosower [16]. Two bands were well characterized in the experimental work: a strong $\pi$–$\pi^*$ and a weak $n$–$\pi^*$ band [16]. Here, we will focus on the long-wavelength $\pi$–$\pi^*$ band and analyze its solvatochromic shift when the MOx change from gas phase to water. On the basis of the experimental transition energies measured for several solvent with different polarities, it is possible to obtain an experimental extrapolation to the gas-phase transition energy. Classifying the solvents used by Kosower [16] with the normalized Reichardt polarity scale [2], $E_T^N$, the solvent with lowest polarity is iso-octane ($E_T^N = 0.012$) and with largest polarity is water ($E_T^N = 1.000$). The $\lambda_{max}$ measured for the MOx in iso-octane is 230.6 ± 0.5 nm (43,365 ± 90 cm$^{-1}$) and in water is 242.6 ± 0.5 nm (41,220 ± 90 cm$^{-1}$) [16]. In Fig. 3, we present a plot of the experimental values for the maximum absorption transition energy, $E_{max}$, of the MOx in several solvent [16] versus the normalized Reichardt solvent polarity scale, $E_T^N$ [2]. Fitting the data with a linear regression, an extrapolation for the $E_{max}$ of MOx in gas phase ($E_T^N = -0.111$) is obtained as 43630 cm$^{-1}$ (229.2 nm). This is only 1.4 nm (265 cm$^{-1}$ = 0.033 eV) lower than the iso-octane value. Therefore, the solvatochromic or bathochromic shift of the $\pi$–$\pi^*$ band of MOx is measured as −2,145 ± 90 cm$^{-1}$ (−0.266 ± 0.011 eV) when the solvent changes from iso-octane to water [16] and extrapolated as −2,410 ± 90 cm$^{-1}$ (−0.299 ± 0.011 eV) from gas phase to water.

TDDFT results for the gas-phase $\pi$–$\pi^*$ electronic excitation energies (in cm$^{-1}$) are gathered in Table 4. The best agreement with the extrapolated experimental gas-phase value of 43,630 cm$^{-1}$ (229.2 nm) is the *syn*-isomer of 43,685 cm$^{-1}$ (228.9 nm) using the B3LYP/6-311+G(d,p), which is inside the experiment precision of 0.5 nm (90 cm$^{-1}$ in this region). For the *anti*-isomer, with the same level of calculation, the electronic excitation was obtained as 44,895 cm$^{-1}$ (222.7 nm). For both properties, dipole moment and excitation energy, the *syn*-isomer calculated values are in better agreement with the experimental values than the *anti*-isomer.

As discussed above assuming a *syn/anti* population of 91:9 % at MP2/aug-cc-pVDZ in the gas phase, the properties can be calculated as weighted averages of the *syn*- and *anti*-isomers. This leads to a calculated gas-phase dipole moment of 2.90 D with MP2/aug-cc-pVDZ and excitation energy of 43,794 cm$^{-1}$ (228.3 nm) with B3LYP/6-311+G(d,p). This represents only a small change of 0.10 D in the dipole moment and of −0.6 nm in the excitation

**Table 4** Gas-phase results for the $\pi$–$\pi^*$ excitation energies ($E$ in $cm^{-1}$) of the *syn*- and *anti*-isomers of the mesityl oxide and the difference between the excitation energies, $\delta E_{syn\rightarrow anti} = E_{anti}(gas) - E_{syn}(gas)$

| | B3LYP | | | BHandHLYP | | | EOM-CCSD | | |
|---|---|---|---|---|---|---|---|---|---|
| | *Syn* | *Anti* | $\delta E_{syn\rightarrow anty}$ | *Syn* | *Anti* | $\delta E_{syn\rightarrow anty}$ | *Syn* | *Anti* | $\delta E_{syn\rightarrow anty}$ |
| 6-31+G(d) | 44,084 | 45,273 | 1,189 | 46,753 | 48,407 | 1,654 | 49,604 | 51,863 | 2,259 |
| 6-311+G(d,p) | 43,783 | 45,031 | 1,248 | 46,414 | 48,114 | 1,700 | | | |
| 6-311++G(d,p) | 43,685 | 44,895 | 1,210 | 46,352 | 48,065 | 1,713 | | | |
| 6-311++G(d,p)[a] | 43,440 | 44,570 | 1,130 | 46,015 | 47,590 | 1,575 | | | |
| 6-311++G(d,p)[b] | 43,580 | 44,590 | 1,010 | 46,205 | 47,675 | 1,470 | | | |
| cc-pVDZ | 44,998 | 46,290 | 1,292 | 47,651 | 49,307 | 1,656 | 51,056 | 53,476 | 2,420 |
| aug-cc-pVDZ | 43,543 | 44,735 | 1,192 | 46,194 | 47,920 | 1,726 | 48,556 | 50,814 | 2,258 |
| aug-cc-pVTZ | 43,510 | 44,725 | 1,215 | 46,134 | 47,858 | 1,724 | | | |
| In iso-octane[c] | 43,365 ± 90 | | | | | | | | |
| In gas phase[d] | 43,630 ± 90 | | | | | | | | |

[a] Results using the MOx geometry optimized in water with PCM model

[b] Results using the MOx geometry optimized in a complex with one hydrogen-bonded water molecule

[c] Experimental value of $E_{max}$ measured in iso-octane [16]

[d] Extrapolated value of $E_{max}$ in gas phase (see Fig. 3)

energy when compared to a population of 100 % of *syn*-isomer in gas phase. Therefore, in this work, for simplification, we assumed a composition of 100 % of MOx *syn*-isomer in gas phase and 100 % of MOx *anti*-isomer in aqueous solution.

The molecular orbitals involved in this $\pi$–$\pi^*$ excitation are the highest occupied molecular orbital (HOMO) to the lowest unoccupied molecular orbital (LUMO). The graphic representations of these molecular orbitals are presented in Fig. 4. As it can be seen, there is a charge transfer character in this HOMO → LUMO excitation: from the $(CH_3)_2C{=}C$ region to the CHCO region. This evidence corroborates the experimental interpretation of the $\pi$–$\pi^*$ band for other molecules of the family of non-saturated $\alpha,\beta$-ketones [18].

At this theoretical level (B3LYP/6-311++G(d,p)), the $\pi$–$\pi^*$ excitation energy for the *anti*-isomer is blue-shifted by 1,210 $cm^{-1}$ (0.15 eV) relative to the *syn*-isomer, $\delta E_{syn\rightarrow anti} = E_{anti}(gas) - E_{syn}(gas)$, as shown in Table 4. It should be observed that this value is quite similar to the one predicted by using the aug-cc-pVTZ basis-set (1,215 $cm^{-1}$). Therefore, the 6–311++G(d,p) basis-set can be a good choice for the calculations in the MOx–water solution since it is computationally less demanding. It should be noticed that gas-phase excitation energies of MOx and the $\delta E_{syn\rightarrow anti}$ exhibit some dependence on the theoretical method and significant deviations from experiment are observed for the B3LYP and BHandHLYP functionals. Using the aug-cc-pVDZ basis-set, the B3LYP predicts a $\delta E_{syn\rightarrow anti}$ of 1,192 $cm^{-1}$ (0.15 eV) and the BHandHLYP predicts a $\delta E_{syn\rightarrow anti}$ of 1,726 $cm^{-1}$ (0.21 eV). But the results also indicate that $\delta E_{syn\rightarrow anti}$ is not very dependent on the basis-set, ranging from 1,189 to 1,292 $cm^{-1}$ using B3LYP and from 1,654 to 1,726 $cm^{-1}$ to BHandHLYP.

In the absence of experimental data for $\delta E_{syn\rightarrow anti}$, it could be of interest to carry out calculations relying on a reference theoretical method to predict excitation energies. EOM-CCSD gas-phase excitation energies for the MOx *syn*- and *anti*-isomers are also reported in Table 4. The EOM-CCSD results indicate that DFT, in particular, the B3LYP exchange–correlation functional, underestimates $\delta E_{syn\rightarrow anti}$. However, the difference between EOM-CCSD (2,258 $cm^{-1}$ = 0.28 eV) and BHandHLYP (1,726 $cm^{-1}$ = 0.21 eV) calculations is quite small (0.07 eV).

The $\pi$–$\pi^*$ excitation energies were also calculated for the MOx geometries optimized in water (using the PCM model and a cluster with one explicit water molecule). These values are also reported in Table 4. The results indicate that the C=O distance stretching induced by the presence of water leads to a small red-shift of the $\pi$–$\pi^*$ excitation energies relative to the values for the isolated optimized geometry. In this case, the $\delta E_{syn\rightarrow anti}$ is 1,575 $cm^{-1}$ (0.20 eV or −7.2 nm) using the optimized geometry with PCM and 1,470 $cm^{-1}$ (0.18 eV or −7.7 nm) using the optimized geometry with one bonded water molecule, both results with BHandHLYP/6-311++G(d,p). Therefore, the inclusion of the MOx relaxation in the presence of the aqueous solution provides a small red-shift of around 100–300 $cm^{-1}$ (0.01–0.04 eV). This result is in concordance with values previously reported for acetone in water [45].

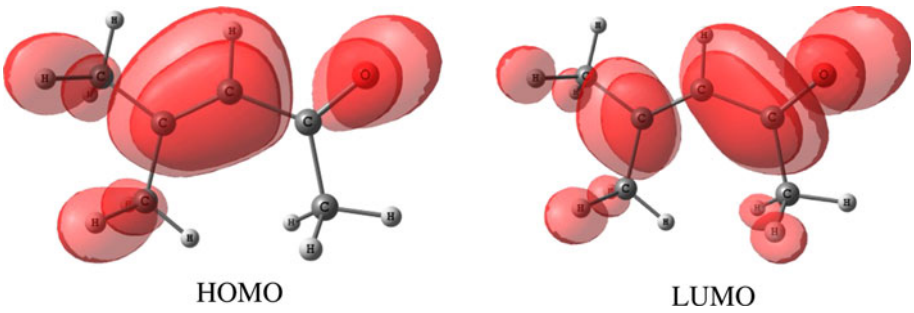


**Fig. 4** Illustration of the frontier molecular orbitals involved in the $\pi$–$\pi^*$ transition: highest occupied molecular orbital (HOMO) and lowest unoccupied molecular orbital (LUMO)

## 3.2 Properties of the mesityl oxide–water solution

### 3.2.1 *Polarization effects of water on hydrated mesityl oxide*

The gas-phase QM calculated dipole moment of the MOx *anti*-isomer (3.90 D) is larger than the *syn*-isomer (2.77 D). In contrast with this, the OPLS charges predict that the *syn*-isomer has a stronger dipole (3.63 D) than the *anti*-isomer (3.10 D), see Table 1. Therefore, these atomic charges are inadequate to be used in molecular simulations. The dipole moments from the polarized procedure using S-QM/MM in water are 4.97 D (*syn*) and 6.96 D (*anti*) and thus correspond to our estimate of the (effective) dipole moments for MOx in water. These three sets of atomic charges and the dipole moments are shown in Table 1. For comparison, the polarized dipole moments of the *syn*- and *anti*-isomers of the MOx were also calculated with the continuum model, PCM, for the water environment. These values are 3.85 D for the *syn*-isomer and 5.25 D for the *anti*-isomer that are around 30 % less than that obtained with the iterative procedure using S-QM/MM method. This is a reasonable result considering that the specific interactions, like the hydrogen-bonded water molecules, are included in the QM calculation as SPC point charges. Therefore, its effect seems to be stronger than that considered in the continuum model.

Figure 5 shows the convergence of the MOx dipole moment during the iterative polarization procedure. Each point in the Fig. 5 corresponds to a QM calculation of the MOx with an embedding represented by an electrostatic average of the solvent (ASEC) [49], where the solvent molecules are considered as point charges. In the present case, this ASEC includes the contribution of 56,250 (= 75 × 250 × 3) point charges from the superposition of 75 statistically uncorrelated configurations with 250 water molecules. As illustrated in Fig. 5, for both isomers, it is observed that an increase of 80 % of the dipole moment relative to the gas-phase value after convergence is attained. The set of atomic charges obtained with this polarization procedure are shown in Table 1.

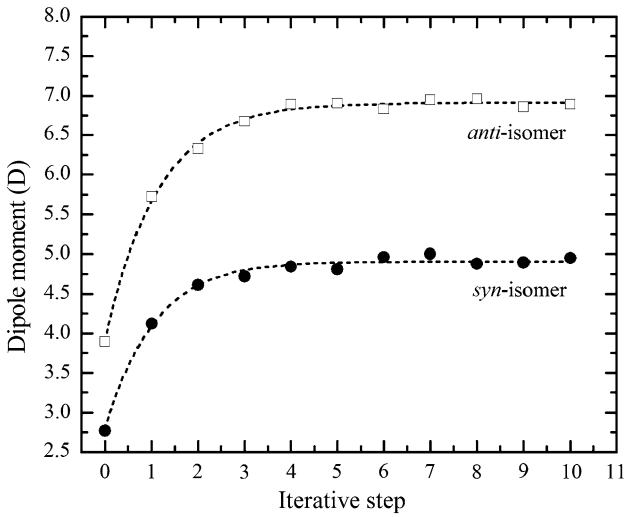


**Fig. 5** Behavior of the mesityl oxide dipole moment in the iterative polarization procedure for the *syn*-isomers (*solid circle*) and *anti*-isomers (*open square*)

### 3.2.2 *Structure and hydrogen bonding in the mesityl oxide–water solution*

The analysis of the structure was carried out by using the configurations generated with the gas-phase atomic charges (non-polarized) and those generated in-water (polarized) atomic charges. The organization of the water around MOx can be discussed through the analysis of the radial distribution function or equivalently by the minimum distance distribution function (MDDF). This distribution corresponds to the histogram calculated with the minimum distance between the atoms of the solute MOx and the atoms of the solvent water molecules and normalized by a parallelogramic uniform distribution [50]. The MDDF is shown in Fig. 6 for the sampling with polarized (bottom) and non-polarized charges (top) and for the *syn*- and *anti*-isomers. The MDDF exhibits a shoulder with a peak at 1.8 Å, which is related to a micro-solvation shell and the hydrogen bond formation (see discussion on hydrogen bonding below). Integration of the MDDF shoulder up to 2.1 Å leads to the number of micro-solvation shell of

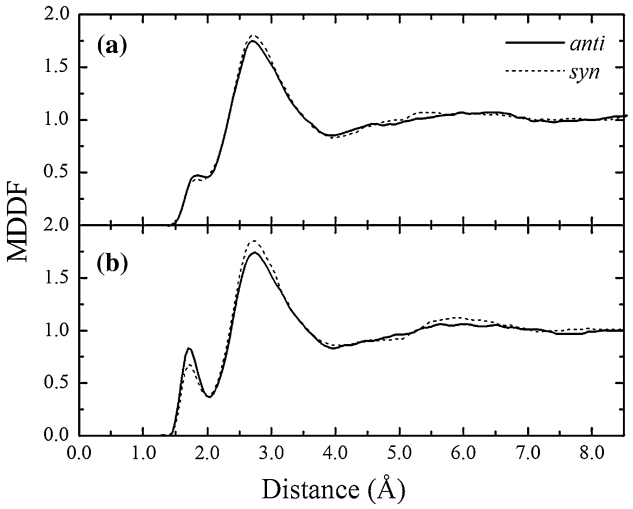


**Fig. 6** Minimum distance distribution function (MDDF) for the *syn* and *anti* mesityl oxide isomers with polarized (**a**) and non-polarized (**b**) atomic charges

approximately 2–3 water molecules, which is also reported in Table 5. Integration of the MDDF up to the first minimum (4.0 Å), that defines the first hydration shell, leads to the first coordination number of 34–35 water molecules. The integration up to the second minimum (7.5 Å), defining a second shell, leads to a second coordination number of 141–145 water molecules. These structural data are gathered in Table 5 for different models and MOx isomers. The results indicate that the organization of the water molecules around the solute is not very dependent on the choice of the charges (non-polarized or polarized). Moreover, with the exception of micro-solvation shell, quite small differences are observed for the water structure around the MOx *syn*- and *anti*-isomers.

The analysis of the hydrogen bond (HB) can be performed using the micro-solvation shell. However, the small distance between the solute–solvent does not fully defines the HB formation. Therefore, the more accurate analysis of the HB should be carried out by defining the geometric and energetic criteria [51, 52]. In this work, we used a distance between the MOx oxygen ($O_M$) and water oxygen ($O_w$), $R(O_M \ldots O_W) \leq 3.25$ Å (value of the first minimum in the $O_MO_W$ RDF), an angle between $O_M$ and $O_WH$, $\theta(O_M \ldots O_WH) \leq 40°$ and a binding energy (calculated by the interaction model) $E_{ij} \leq -0.01$ kcal/mol. This energy criterion is used only to guarantee that the water molecule is binding to the MOx. Using these criteria, the results for the statistical analysis on HB distribution and the average properties of HB in the MOx–water solution and its standard deviation are reported also in Table 5. The following specific aspects are worth noticing. For both non-polarized and polarized charges, the percentage of water molecules with only one hydrogen bond (1 HB) to MOx is dominant. If we consider the *syn*-isomer, the numbers are 55.3 and 42.7 % for non-polarized and polarized charges, respectively. However, comparison between the *syn*- and *anti*-isomers shows that in contrast with the results for the non-polarized charges, polarized leads to quite similar populations for both isomers (42.7 %) and a significant change on the number of water molecules with two hydrogen bonds (2 HB) to MOx. The fraction of configurations with three hydrogen bonds (3 HB) is quite small.

**Table 5** Number of water molecules in the micro-, first and second solvation shells and the hydrogen-bonded (HB) to the mesityl oxide, and the statistical analysis (average and standard deviation values) of HB properties for two different charge distribution models used in the MC simulations: non-polarized (gas phase) and polarized in water (see Table 1)

| | Non-polarized | | Polarized | |
|---|---|---|---|---|
| | *Syn* | *Anti* | *Syn* | *Anti* |
| *Number of water molecules* | | | | |
| Micro-solvation shell (up to 2.1 Å) | 1.9 | 1.9 | 2.4 | 2.8 |
| 1st shell (up to 4.0 Å) | 34 | 34 | 35 | 35 |
| 2nd shell (up to 7.5 Å) | 143 | 141 | 145 | 143 |
| *% of Configurations with* | | | | |
| 0 HB | 36.3 | 35.6 | 22.1 | 0.4 |
| 1 HB | 55.3 | 44.0 | 42.7 | 42.7 |
| 2 HB | 8.4 | 28.8 | 33.5 | 55.3 |
| 3 HB | 0.0 | 1.6 | 1.7 | 1.6 |
| *HB average properties* | | | | |
| Number of water $\langle N_{HB} \rangle$ | 0.7 | 1.1 | 1.2 | 1.6 |
| Distance $\langle R(O_M \ldots O_W) \rangle$ (in Å) | 2.82 ± 0.15 | 2.82 ± 0.16 | 2.74 ± 0.15 | 2.75 ± 0.16 |
| Angle $\langle \theta(O_M \ldots O_WH) \rangle$ (in °) | 15 ± 9 | 15 ± 9 | 12 ± 7 | 12 ± 7 |
| Energy $\langle E_{ij} \rangle$ (in kcal/mol) | −4.9 ± 1.2 | −4.8 ± 1.2 | −7.3 ± 1.5 | −8.2 ± 1.5 |

These results are not surprising if we take into account the increase of the charges (and dipole moment) of MOx in water when a polarization procedure is adopted to estimate the charge distribution (see Fig. 5 and Table 1). By taking the average of the HB, $\langle N_{HB} \rangle$, for the different isomers, we conclude that they are of $\sim 1$ and $\sim 1.5$ for the *syn*- and *anti*-isomers, respectively. Therefore, the polarization effect does not increase significantly the quantity of HB (only 0.5 HB), but makes it more oriented, shorter and stronger, as it can be seen in Table 5. For the *anti*-isomer, the HB O…O distance decreases from 2.82 to 2.75 Å, the O…OH angle decreases from 15° to 12°, and the binding energy increases from 4.8 kcal/mol to 8.2 kcal/mol for the non-polarized and the polarized models, respectively. These results show the relevance of using a polarized model for the solute.

### 3.2.3 *Gibbs free energy and conformational change of mesityl oxide in water*

The conformational equilibrium in solution was investigated by calculating the Gibbs free energy change associated with the interconversions between different isomers (*syn* and *anti*) and with the transition state structure (TS). The Gibbs free energy change in aqueous solution $\Delta G_{x\to y}(aq)$ can be determined through the definition of a thermodynamic cycle and estimated as:

$$\begin{aligned}\Delta G_{x\to y}(aq) &= \Delta G_{x\to y}(gas) + (\Delta G_x(aq) - \Delta G_y(aq)) \\ &= \Delta G_{x\to y}(gas) + \Delta\Delta G_{x\to y}(aq)\end{aligned} \quad (1)$$

where $x$ and $y$ represent the different solutes (*syn*, *anti* and TS), $\Delta G_x(aq)$ is the Gibbs free energy of hydration associated with the species $x$ (calculated by TPT), $\Delta\Delta G_{x\to y}(aq)$ is the differential free energy of hydration, and $\Delta G_{x\to y}(gas)$ is the gas-phase free energy difference that can be evaluated by QM methods (see Table 3). Moreover, it is possible to separate the different contributions (electrostatic and non-electrostatic) to the total $\Delta G_x(aq)$ [43, 44]. Once, the $\Delta G_x(aq) = -\Delta G_{x\to 0}(aq)$, where $\Delta G_{x\to 0}(aq)$ is the free energy of annihilation of the species $x$ in aqueous solution. This annihilation process is divided in two parts: first the Coulombic potential is annihilated then the Lennard-Jones potential. All the calculated values of these variations of free energy are presented in Table 6. For comparison, the free energies of hydration of the MOx were also calculated with the continuum model, PCM, for the water environment and are shown in Table 6. Only for these QM calculations of the solvation free energy, the PCM was

**Table 6** Non-electrostatic and electrostatic contributions to the Gibbs free energy of hydration, $\Delta G_x(aq)$, the total hydration free energy, $\Delta\Delta G_{x\to y}(aq)$, and the Gibbs free energy change in aqueous solution, $\Delta G_{x\to y}(aq)$, of the MOx isomers (*syn* and *anti*) and transition state structure (TS) obtained with QM calculation with PCM-UAHF(HF/6-31G(d)) and with TPT in the MC simulations

| | *Syn* | TS | *Anti* |
|---|---|---|---|
| *QM continuum model, PCM-UAHF* | | | |
| $\Delta G_x(aq)$ non-electrostatic contribution | 2.19 | 2.73 | 2.22 |
| $\Delta G_x(aq)$ electrostatic contribution | −5.96 | −6.90 | −7.49 |
| Total $\Delta G_x(aq)$ | −3.77 | −4.17 | −5.27 |
| | | *Syn* → TS | *Syn* → *anti* |
| $\Delta\Delta G_{x\to y}(aq)$ | | −0.40 | −1.50 |
| | | −0.20[a]; −0.39[b] | −1.27[a]; −1.43[b] |
| $\Delta G_{x\to y}$ (aq)[c] | | 3.17 | −0.16 |
| | *Syn* | TS | *Anti* |
| TPT in MC simulation | | | |
| $\Delta G_x$ (aq) non-electrostatic contribution | −0.64 ± 0.03 | −1.12 ± 0.06 | −1.26 ± 0.06 |
| $\Delta G_x$ (aq) electrostatic contribution | −12.71 ± 0.64 | −12.79 ± 0.63 | −16.20 ± 0.80 |
| Total $\Delta G_x$ (aq) | −13.35 ± 0.67 | −13.91 ± 0.69 | −17.46 ± 0.86 |
| | | *Syn* → TS | *Syn* → *anti* |
| $\Delta\Delta G_{x\to y}$ (aq) | | −0.56 ± 0.96 | −4.11 ± 1.09 |
| $\Delta G_{x\to y}$ (aq)[c] | | 3.01 ± 0.96 | −2.77 ± 1.09 (99 %) |

All values are in kcal/mol, and the deviations are the statistical error. The population of the *anti*-isomer in water is reported in the parenthesis

[a] Obtained with PCM-UAHF(B3LYP/aug-cc-pVDZ)

[b] Obtained with PCM-UAHF(MP2/aug-cc-pVDZ)

[c] Obtained from the thermodynamic cycle (see Eq. 1) with $\Delta G_{x\to y}$ (gas) using MP2/aug-cc-pVDZ (see Table 3)

performed using the united atom topological model applied on atomic radii optimized for the HF/6-31G(d) level of theory (UAHF). This UAHF radii option is consistent with the non-electrostatic parametrized terms of the solvation free energy implemented in Gaussian program and gives the best performance when compared with the experimental results [53, 54].

It should be noticed that the free energy of hydration, $\Delta G_x$(aq), of MOx conformations (*syn*, *TS* and *anti*) exhibits some dependence on the theoretical method. In Table 6, comparing the non-electrostatic contribution obtained with PCM solvent model (all positive values) and with TPT in simulation (all negative values), it seems that the PCM is underestimating the van der Waals and dispersion interactions (negative contributions to the free energy of hydration) or super estimating the cavitation contribution (positive contributions to the free energy of hydration), or both. Additionally, comparing the electrostatic contribution, we believe that the PCM solvent model is underestimating the in-water polarization of the MOx, as described in previous section. Therefore, all the electrostatic contribution values obtained with PCM are smaller than with TPT. However, for all used method, the *anti*-isomer solvates better in water solution than the *syn*-isomer by around 4 kcal/mol using TPT in simulations and 1.5 kcal/mol using QM calculations with PCM-UAHF. Using the QM calculations for $\Delta G_{x\rightarrow y}$(gas) reported in Table 3 (best result with MP2/aug-cc-pVDZ) and Eq. (1), the free energy change in water, $\Delta G_{x\rightarrow y}$(aq), can be estimated and the results are also reported in Table 6. Based on the results for $\Delta G_{x\rightarrow y}$(aq) calculated with TPT, the *anti*-isomer is dominant in the aqueous solution by more than 99 % of population. These results show that the *syn–anti* equilibrium of the MOx is solvent dependent and it is in agreement with the citation of Kosower [16].

### 3.2.4 Absorption spectrum of mesityl oxide in water

According with experimental data, the $\pi$–$\pi^*$ band of MOx is shifted by $-2{,}145 \pm 90$ cm$^{-1}$ ($-0.266 \pm 0.011$ eV) when the solvent changes from iso-octane to water [16] and extrapolated as $-2{,}410 \pm 90$ cm$^{-1}$ ($-0.299 \pm 0.011$ eV) from gas phase to water using a linear regression in the a plot of the experimental values for the maximum absorption transition energy, $E_{max}$, of the MOx in several solvent [16] versus the normalized Reichardt solvent polarity scale, $E_T^N$ [2] (see Fig. 3). In order to discuss, the absorption spectrum of solute MOx (S) in water different theoretical representations of the solvent was adopted: (1) the polarizable continuum model (S + PCM), which provides a simplified representation of the solvent as a continuum dielectric medium; (2) the average solvent electrostatic configuration (S + ASEC), where 250 water molecules of

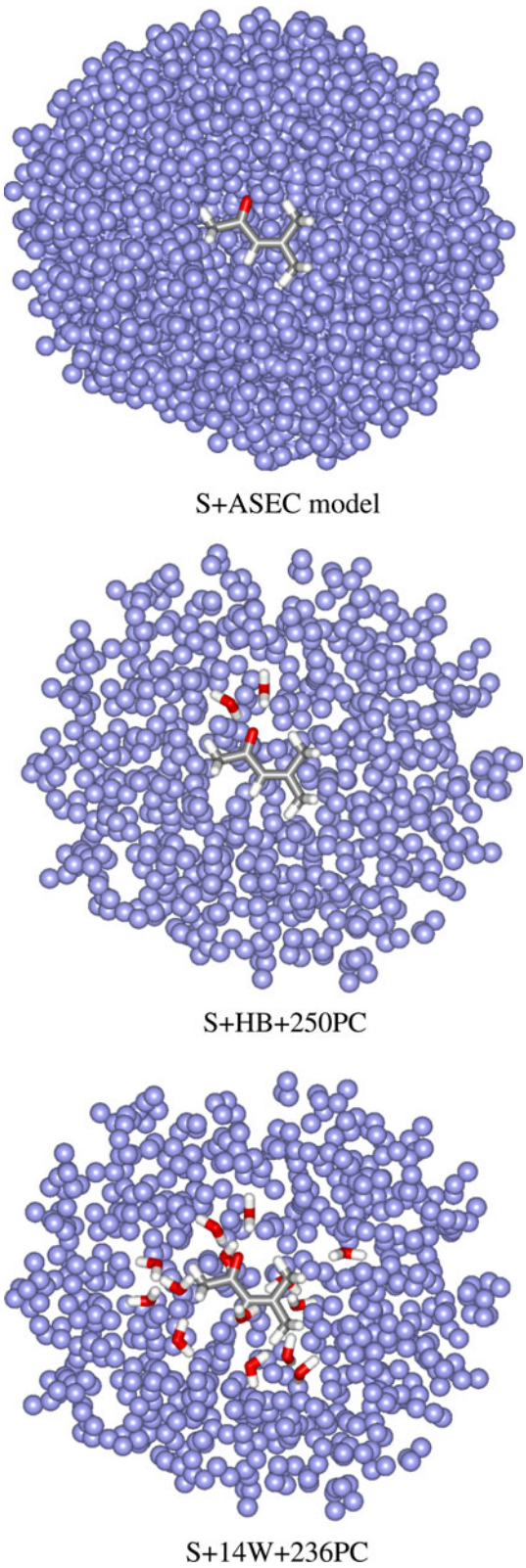


**Fig. 7** An illustration of the models used in the QM calculation: S+ASEC, one configuration of S+HB+250PC and one configuration of S+14W+236PC. The point charges are represented by small spheres

**Table 7** Solvent effect on the $\pi$–$\pi^*$ excitation of mesityl oxide

| Model | $\Delta E_{syn}$ | | $\Delta E_{anti}$ | | $\Delta E_{syn\rightarrow anti}$ | |
|---|---|---|---|---|---|---|
| | B3LYP | BHandHLYP | B3LYP | BHandHLYP | B3LYP | BHandHLYP |
| S+PCM | −1,510 | −1,551 | −1,855 | −2,088 | −645 | −375 |
| S+ASEC | −1,645 | −1,615 | −2,385 | −2,526 | −1,175 | −813 |
| S+HB+250PC | −2,129 ± 59 | −2,021 ± 60 | −3,025 ± 85 | −3,022 ± 70 | −1,815 ± 85 | −1,309 ± 70 |
| S+8W+242PC | −3,039 ± 112 | −2,644 ± 71 | −4,077 ± 92 | −3,979 ± 83 | −2,867 ± 92 | −2,266 ± 83 |
| S+12W+238PC | −3,187 ± 85 | −2,777 ± 72 | −4,356 ± 101 | −4,156 ± 87 | −3,146 ± 101 | −2,443 ± 87 |
| S+14W+236PC | −3,256 ± 83 | −2,810 ± 73 | −4,459 ± 115 | −4,232 ± 88 | −3,249 ± 115 | −2,519 ± 88 |
| Experimental shift of iso-octane to water [16] | | | | | | −2,145 ± 90 |
| Extrapolated shift of gas phase to water (see Fig. 3) | | | | | | −2,410 ± 90 |

$\Delta E = E(\text{aq}) - E(\text{gas})$ where $E$(aq) and $E$(gas) are the excitation energies in aqueous solution and gas phase, respectively. TDDFT calculations with the 6-311++G(d,p) basis-set. $\Delta E_x$ values assume both, $E$(aq) and $E$(gas), in the $x$-isomer, and the $\Delta E_{syn\rightarrow anti}$ values considered the excitation energy difference between the gas-phase MOx in the *syn*-isomer and the in-water MOx in the *anti*-isomers and represent the total solvent effect on the $\pi$–$\pi^*$ excitation. The description of the models is as follows: *S* MOx solute molecule, *PCM* the polarizable continuum model, *ASEC* the average solvent electrostatic configuration, where the 250 water molecules of 75 configurations are represented as point charges, *HB* the hydrogen-bonded water molecules explicitly included in the QM calculation, *nW* the nearest $n$ water molecules explicitly included in the QM calculation, where $n = 8$, 12 and 14, *mPC* remaining $m$ water molecules described by point charges, where $m = 242$, 238 and 236. For all $n$W + $m$PC models, the nearest 250 water molecules were used ($n + m = 250$). All values are in $\text{cm}^{-1}$

75 configurations are superposed and represented as re-scaled point charges; (3) the hydrogen bond model (S+HB+250PC) that includes explicitly a few water molecules hydrogen-bonded to MOx (in average 1.2 for the *syn*-isomer and 1.6 for the *anti*-isomer, see Table 5) and this system is embedded in the electrostatic field of the remained 250 water molecules represented by point charges (250PC); and (*iv*) the explicit model (S+$n$W+$m$PC) where the nearest $n$ water molecules to MOx ($n$W) are explicitly included in the calculation, where $n = 8$, 12 and 14, and this system is embedded in the electrostatic field of the remained solvent molecules represented by $m$ point charges, where $m = 242$, 238 and 236. For all S+$n$W+$m$PC models, the nearest 250 water molecules were used ($n + m = 250$). In Fig. 7, we show an illustration of the S+ASEC model (top), one configuration of the S+HB+250PC (center) and S+14W+236PC (bottom) models. Note that for the S+PCM and S+ASEC models, only one QM calculation is performed to obtain the $\pi$–$\pi^*$ excitation energy of the MOx in water because both models represent the solvent average behavior. But for the S+HB+250PC and S+$n$W+$m$PC models, the $\pi$–$\pi^*$ excitation energy of the MOx in water is obtained as an average over 75 statistically uncorrelated configurations generated from the MC simulations.

The shift of the $\pi$–$\pi^*$ excitation energy of the MOx upon hydration, considering the *syn* → *anti* isomerization change, is

$$\Delta E_{syn\rightarrow anti} = E_{anti}(\text{aq}) - E_{syn}(\text{gas}), \quad (2)$$

where $E_{anti}(aq)$ is the excitation energy of the hydrated MOx *anti*-isomer, and $E_{syn}(gas)$ is the excitation energy of the isolated MOx *syn*-isomer. This expression can be re-written as

$$\begin{aligned}\Delta E_{syn\rightarrow anti} &= (E_{anti}(\text{gas}) + \Delta E_{anti}) - E_{syn}(\text{gas}) \\ &= \delta E_{syn\rightarrow anti} + \Delta E_{anti}, \end{aligned} \quad (3)$$

where $\Delta E_{anti} = E_{anti}(\text{aq}) - E_{anti}(\text{gas})$ is the excitation energy shift due to the solvent effect on electronic structure of the specific *anti*-isomer, and $\delta E_{syn\rightarrow anti} = E_{anti}(\text{gas}) - E_{syn}(\text{gas})$ is the excitation energy shift due to the isomerization change. The $\Delta E_x$ values are reported in Table 7, where $x$ is the *syn*- and *anti*-isomers and the $\delta E_{syn\rightarrow anti}$ are reported in Table 4. Therefore, on the basis of Eq. (3), the analysis of the solvent effect on the MOx excitation spectrum should take into consideration two distinct and opposite contributions. The first one is related to the *syn* → *anti* conformational change leading to a blue-shift of 1,210 $\text{cm}^{-1}$ [1,713 $\text{cm}^{-1}$] for B3LYP [BHandHLYP] calculations with the 6–311++G(d,p) basis-set (see Table 4). The second contribution is related to the solvent effect and leads to a red-shift of the excitation energy. The results reported in Table 7 for $\Delta E_x$ are in keeping with the experimentally observed trend that points out to a red-shift of the excitation energy when we move from a low- (iso-octane) to a high-polarity solvent (water). However, the magnitude of $\Delta E_x$ is clearly dependent on of the adopted procedure to represent the solvent effect. In the specific case of the *anti*-isomer and for BHandHLYP calculations, $\Delta E_{anti}$ changes from −2,088 $\text{cm}^{-1}$ (PCM) to −4,232 ± 88 $\text{cm}^{-1}$ for the model S+14W+236PC, where the solute is in interaction with 14 (explicit) water molecules embedded in the electrostatic field of 236 water molecules represented as point charges. Moreover, it appears that $\Delta E$ is also dependent on the number ($m$W) of water molecules explicitly included in the calculations. However, the difference between the results with 12 and 14 explicit water

molecules (76 $cm^{-1}$ using BHandHLYP and 103 $cm^{-1}$ using B3LYP for the *anti*-isomer) indicates that $\Delta E_x$ is near convergence with 14 W. Therefore, it will be assumed that our best estimate for $\Delta E_x$ relies on the (S+14W+236PC) calculation.

According to Eq. (3) by adding to $\Delta E_{anti}$ the contribution from the gas-phase *syn* → *anti* isomerization ($\delta E_{syn \to anti} = 1{,}210$ and 1,713 $cm^{-1}$, for B3LYP and BHandHLYP, respectively), the total solvatochromism on the MOx $\pi$–$\pi^*$ excitation energy is a red-shift of -3,249 ± 115 $cm^{-1}$ using B3LYP and −2,519 ± 88 $cm^{-1}$ using BHandHLYP, whereas the experimental extrapolated value is −2,410 ± 90 $cm^{-1}$. Our theoretical estimate (using BHandHLYP) is red-shifted by only 109 $cm^{-1}$ (0.014 eV) from the extrapolated experimental result and indicates that our best approximation for representing the solvent effect on the MOx $\pi$–$\pi^*$ excitation is adequate.

## 4 Conclusions

Sequential QM/MM calculations were carried out to investigate the hydration of a model non-saturated $\alpha,\beta$-ketone. Our main conclusions are the following. The *syn–anti* equilibrium of mesityl oxide (MOx) is solvent dependent. In gas-phase and low-polarity solvents, it exists dominantly in *syn*-form and in aqueous solution in *anti*-form. This conclusion is supported by Gibbs free energy calculations in gas phase and in-water by applying quantum mechanical calculations with polarizable continuum model and thermodynamic perturbation theory in Monte Carlo simulations using a polarized MOx model. The consideration of the in-water polarization of the MOx is very important to correctly describe the solute–solvent electrostatic interaction. We predict that the dipole moment of MOx in water is ∼5 D for the *syn*-isomer and ∼7 D for the *anti*-isomer. It represents an increase of 2.2 D in the *syn*-isomer and 3.1 D the *anti*-isomer compared to the gas-phase MOx. Statistical analysis of MOx–water hydrogen bonding and comparison between polarized and non-polarized models indicate that by using polarized charges on the solute, the number of configurations with two water molecules hydrogen-bonded to MOx (*anti*) is increased by ∼26 % and the hydrogen bonds became ∼70 % stronger relative to the non-polarized model. Our best estimate for the shift of the $\pi$–$\pi^*$ transition energy of MOx, when it changes from gas-phase to water solvent, shows a red-shift of −2,520 ± 90 $cm^{-1}$, which is only 109 $cm^{-1}$ (0.014 eV) below experimental extrapolation of −2,410 ± 90 $cm^{-1}$. Therefore, this red-shift of around −2,500 $cm^{-1}$ can be divided in two distinct and opposite contributions. One contribution is related to the *syn* → *anti* conformational change leading to a blue-shift of ∼1,700 $cm^{-1}$. Other contribution is the solvent effect on the electronic structure of the MOx leading to a red-shift of around −4,200 $cm^{-1}$. Additionally, this red-shift caused by the solvent effect on the electronic structure (∼4,200 $cm^{-1}$) can be composed by approximately 60 % due to the electrostatic bulk effect (∼2,500 $cm^{-1}$), 10 % due to the explicit inclusion of the hydrogen-bonded water molecules (∼500 $cm^{-1}$) and 30 % due to the explicit inclusion of the nearest water molecules (∼1,200 $cm^{-1}$). The set of information on the structure, thermodynamics and electronic properties of MOx in water stresses the interest of performing theoretical studies that combine statistical, molecular and quantum mechanics with explicit solvent molecules for investigating solvent effects.

**Acknowledgments** Work partially supported by FCT (Portugal), CNPq, CAPES, FAPESP, INCT-FCx and nBioNet (Brazil).

## References

1. Reichardt C (1979) Solvent effects in organic chemistry. Verlag Chemie, Weinheim, New York
2. Reichardt C (1994) Chem Rev 94:2319
3. Maitland GC, Rigby M, Smith EB, Wakeham WA (1987) Intermolecular forces-their origin and determination. Oxford University Press, Oxford
4. Ratajczak H, Orville-Thomas WJ (1980–1982) Molecular Interactions. vol. 1-3 Wiley, New York
5. Timasheff SN (1970) Acc Chem Res 3:62
6. Suppan P, Ghoneim N (1997) Solvatochromism. The Royal Society of Chemistry, London
7. Sheppard SE (1942) Rev Mod Phys 14:303
8. Archer WL (1996) Industrial solvents handbook. Dekker, New York
9. Reichardt C (1965) Angew Chem 4:29
10. Novaki PL, El Soud OA (1997) Ber Bunsenges Phys Chem 101:902
11. Kosower EM (1968) An introduction to physical organic chemistry. Wiley, New York
12. Streitwieser A, Heathcock CH, Kosower EM (1992) Introduction to organic chemistry. McMillan, New York
13. Buckingham DA, Lippert E, Bratos E (eds) (1978) Organic liquids—structure, dynamics and chemical properties. Wiley, New York
14. Stross FH, Monger JM, Finch HV (1947) J Am Chem Soc 69:1627
15. Gray HF Jr, Rasmussen RS, Tunnicliff DD (1947) J Am Chem Soc 69:1630
16. Kosower EM (1958) J Am Chem Soc 80:3261
17. Woodward RB (1941) J Am Chem Soc 63:1123
18. Turner RB, Voitle DM (1951) J Am Chem Soc 73:1403
19. Forbes WF, Shilton R (1959) J Am Chem Soc 81:786
20. Coutinho K, Canuto S (2000) J Chem Phys 113:9132
21. Coutinho K, Canuto S, Zerner MC (2000) J Chem Phys 112:9874
22. Parr RG, Yang W (1994) Density functional theory of atoms and molecules. Oxford Science Publications, Oxford
23. Becke AD (1993) J Chem Phys 98:5648
24. Imamura Y, Otsuka T, Nakai H (2007) J Comput Chem 28:2067
25. Møller C, Plesset MS (1934) Phys Rev 46:618

26. Krishnan R, Pople JA (1978) Int J Quantum Chem 14:91
27. Ditchfield D, Hehre WJ, Pople JA (1971) J Chem Phys 54:724
28. Dunning Jr TH(1987) J Chem Phys 90:1007
29. Fiolhais C, Nogueira F, Marques M (eds) (2003) A primer in density functional theory. Chapter 4, Springer, New York
30. Frisch MJ, Trucks GW, Schlegel HB, Scuseria GE, Robb MA, Cheeseman JR, Montgomery JA, Vreven T, Kudin KN, Burant JC, Millam JM, Iyengar SS, Tomasi J, Barone V, Mennucci B, Coss M, Scalmani G, Rega N, Petersson GA, Nakatsuji H, Hada M, Ehara M, Toyota K, Fukuda R, Hasegawa J, Ishida M, Nakajima T, Honda Y, Kitao O, Nakai H, Klene M, Li X, Knox JE, Hratchian HP, Cross JB, Bakken V, Adamo C, Jaramillo J, Gomperts R, Stratmann RE, Yazyev O, Austin AJ, Cammi R, Pomelli C, Ochterski JW, Ayala PY, Morokuma K, Voth GA, Salvador P, Dannenberg JJ, Zakrzewski VG, Dapprich S, Daniels AD, Strain MC, Farkas O, Malick DK, Rabuck AD, Raghavachari K, Foresman JB, Ortiz JV, Cui Q, Baboul AG, Clifford S, Cioslowski J, Stefanov BB, Liu G, Liashenko A, Piskorz P, Komaromi I, Martin RL, Fox DJ, Keith T, Al-Laham MA, Peng CY, Nanayakkara A, Challacombe M, Gill PMW, Johnson B, Chen W, Wong MW, Gonzalez C, Pople JA(2004) Gaussian 03, Revision D.01. Gaussian, Inc., Wallingford CT
31. Stanton JF, Bartlett RJ (1993) J Chem Phys 98:7029
32. Miertus S, Scrocco E, Tomasi J (1981) J Chem Phys 55:117
33. Cancès MT, Mennucci B, Tomasi J (1997) J Chem Phys 107:3032
34. Metropolis N, Rosenbluth AW, Rosenbluth MN, Teller AH, Teller E (1953) J Chem Phys 21:1087
35. Coutinho K, Canuto S (2009) DICE: a monte carlo program for molecular liquid simulation, v. 2.9. University of São Paulo, São Paulo
36. Allen MP, Tildesley DJ (1987) Computer simulation of liquids. Clarendon, Oxford
37. Berendsen HJC, Postma JPM, van Gunsteren WF, Hermans J (1981) In: Pullman B (ed) Intermolecular forces. Reidel, Dordrecht
38. Jorgensen WL, Maxwell DS, Tirado-Rives J (1996) J Am Chem Soc 118:11225
39. Georg HC, Coutinho K, Canuto S (2006) Chem Phys Lett 429:119
40. Breneman CM, Wiberg KB (1990) J Comp Chem 11:361
41. Zwanzig RW (1954) J Chem Phys 22:1420
42. Jorgensen WL, Buckner KJ, Boudon S, Tirado-Rives J (1988) J Chem Phys 89:3742
43. Georg HC, Coutinho K, Canuto S (2005) Chem Phys Lett 413:16
44. Pasalic H, Aquino AJA, Tunega D, Haberhauer G, Gerzabek MH, Georg HC, Moraes TF, Coutinho K, Canuto S, Lischka H (2010) J Comp Chem 31:2046
45. Coutinho K, Saavedra N, Canuto S (1999) J Mol Struct (Theochem) 466(1999):69
46. Estok GK, Sikes JH (1953) J Am Chem Soc 75:2745
47. Bentley JB, Everard KB, Marsden RJB, Sutton LE (1949) J Chem Soc 2957. doi:10.1039/JR9490002957
48. Mecke R, Noack K (1960) Chem Ber 93:210
49. Coutinho K, Georg HC, Fonseca TL, Ludwig V, Canuto S (2007) Chem Phys Lett 437:148
50. Georg HC, Coutinho K, Canuto S (2007) J Chem Phys 126:34507
51. Mezei M, Beveridge DL (1981) J Chem Phys 74:622
52. Sceats MG, Rice SA (1981) J Chem Phys 72:3236
53. Barone V, Cossi M, Tomasi J (1997) J Chem Phys 107:3210
54. Ho J, Klamt A, Coote ML (2010) J Phys Chem A 114:13442